



Available online at www.sciencedirect.com

ScienceDirect

Advances in Space Research 58 (2016) 310–325

**ADVANCES IN
SPACE
RESEARCH**
(*a COSPAR publication*)
www.elsevier.com/locate/asr

Atmospheric correction in time-series SAR interferometry for land surface deformation mapping – A case study of Taiyuan, China

Wei Tang ^a, Mingsheng Liao ^{a,b,*}, Peng Yuan ^c

^a State Key Laboratory of Information Engineering in Surveying, Mapping and Remote Sensing, Wuhan University, Wuhan 430079, China

^b Collaborative Innovation Center for Geospatial Technology, Wuhan University, Wuhan 430079, China

^c Research Centre of GNSS, Wuhan University, Wuhan 430079, China

Received 20 December 2015; received in revised form 5 May 2016; accepted 5 May 2016

Available online 11 May 2016

Abstract

The dominant error source of Synthetic Aperture Radar Interferometry (InSAR) is atmospheric phase screen (APS), resulting in phase delay of the radar signal propagating through the atmosphere. The APS in the atmosphere can be decomposed into stratified and turbulent components. In this paper, we introduced a method to compensate for stratified component in a radar interferogram using ERA-Interim reanalysis products obtained from European Centre for Medium-Range Weather Forecasts (ECMWF). Our comparative results with radiosonde data demonstrated that atmospheric condition from ERA-Interim could produce reasonable patterns of vertical profiles of atmospheric states. The stratified atmosphere shows seasonal changes which are correlated with time. It cannot be properly estimated by temporal high-pass filtering which assumes that atmospheric effects are random in time in conventional persistent scatterer InSAR (PSI). Thus, the estimated deformation velocity fields are biased. Therefore, we propose the atmosphere-corrected PSI method that the stratified delay are corrected on each interferogram by using ERA-Interim. The atmospheric residuals after correction of stratified delay were interpreted as random variations in space and time which are mitigated by using spatial-temporal filtering. We applied the proposed method to ENVISAT ASAR images covering Taiyuan basin, China, to study the ground deformation associated with groundwater withdrawal. Experimental results show that the proposed method significantly mitigate the topography-correlated APS and the estimated ground displacements agree more closely with GPS measurements than the conventional PSI.

© 2016 COSPAR. Published by Elsevier Ltd. All rights reserved.

Keywords: InSAR; APS; Persistent scatterer interferometry; Taiyuan basin; Land subsidence

1. Introduction

Synthetic Aperture Radar Interferometry (InSAR) is a satellite-based technique that allows to precisely measure the surface displacement produced by several phenomena like earthquakes, volcanic eruptions, landslides, and land subsidence (Colesanti and Wasowski, 2006; Lanari et al., 1998; Massonnet et al., 1997; Zebker et al., 1994).

Atmospheric phase screen (APS) is one of the main systematic errors in InSAR measurements; severely undermining the accuracy of displacement information.

APS is mainly caused by spatial and temporal variations of air refractivity in the neutral troposphere. Air refractivity variations in the troposphere are related to changes in atmospheric variables such as air temperature, atmospheric pressure, and water vapor content. For short spatial scales less than 50 km, the dominant APS is caused by atmospheric water vapor in the lower part of troposphere (1.5 km). The APS in the troposphere can be categorized into two components: stratified APS and turbulent APS. The stratified APS results from the different vertical

* Corresponding author at: State Key Laboratory of Information Engineering in Surveying, Mapping and Remote Sensing, Wuhan University, Wuhan 430079, China. Tel.: +86 27 68778070.

E-mail address: liao@whu.edu.cn (M. Liao).

refractivity profiles during the two SAR acquisitions and affects mountainous terrain only so that it is strongly correlated with topography. The turbulent APS is the result of turbulent process in the atmosphere. It causes 3D heterogeneity in the refractivity during the SAR acquisitions, and affects flat terrain as well as mountainous terrain (Hanssen, 2001).

Numerous correction methods have been developed to minimize atmospheric effects. One type of approach is assuming a linear relationship between elevation and interferometric phase, thus the atmospheric phase depend on altitude can be estimated from the interferogram itself (Cavalié et al., 2007). Unfortunately, if the expected deformation signal correlates with elevation, the deformation phase and the atmospheric phase are difficult to be discriminated. Another correction method employs the integral water vapor provided by near-IR sensors such as the Medium-Resolution Imaging Spectrometer (MERIS) and the Moderate-Resolution Imaging Spectroradiometer (MODIS) (Li et al., 2005, 2006b). The two sensors have been successfully used to map the lateral heterogeneities in precipitable water vapor content from ground to satellite. Limitations to using satellite multispectral data are the inability to make measurements at night and in the presence of clouds. The wet delay observations from ground GNSS (Global Navigation Satellite Systems) network can also be used to correct APS in InSAR (Li et al., 2006a; Onn and Zebker, 2006). The obvious drawback of using continuous GNSS network is that it is only useful when a dense network exists.

Recently, several researches profited from the use of Global Atmospheric Model (GAM) to predict atmospheric delays at SAR acquisition times and to correct for stratified delay (Doin et al., 2009; Jolivet et al., 2011). GAM provides vertical profiles of atmospheric parameters such as temperature, specific/relative humidity, and geopotential height on a regular spatial grid at regular time steps. Using these parameters, we can apply the refractivity equations to determine the atmospheric path delays. The advantage of this technique is to mitigate the atmospheric phase distortion on a scene-to-scene basis regardless of cloud presence.

In contrast to the methods which based on auxiliary data for atmospheric correction, interferometric combination of a series of SAR (Synthetic Aperture Radar) acquisitions can be used to identify atmospheric artifacts. The main idea of these methods for isolating the atmospheric artifacts from the deformation signal is based on the assumption that the atmospheric influence is randomly in time, whereas deformation signal correlates with time (Berardino et al., 2002; Ferretti et al., 2001; Hooper et al., 2007). Thus, it is suggested that the atmospheric effect can be mitigated by temporal filtering of large time series SAR images. However, this assumption is not always valid for stratified APS component because the seasonal oscillation of the atmospheric conditions are not well sampled in time by temporal filtering. The remained residuals

would bias the velocity fields estimated by those conventional time series analysis methods.

In this paper, we propose an efficient method to correct stratified delay by using ERA-Interim products from European Centre for Medium-Range Weather Forecasts (ECMWF) and incorporate this atmospheric correction method into persistent scatterer InSAR (PSI) (Hooper, Segall, 2007) (called atmosphere-corrected PSI). The residuals containing turbulent component of atmospheric effects are considered as a random signal in time and estimated by spatial-temporal filtering in further time series analysis. We illustrated the proposed method on the ENVISAT time series of SAR data covering Taiyuan basin, China.

2. Atmospheric phase delay correction using ERA-Interim

2.1. Atmospheric delay in InSAR

The variations of the air refractivity cause phase delay when the electromagnetic signals propagate through the atmosphere. Based on the formulation of (Baby et al., 1988), the zenith total delay can be calculated and then be converted to the total delay in the satellite line-of-sight (LOS) direction:

$$\delta L_{\text{LOS}}^{\text{total}}(z) = \frac{10^{-6}}{\cos(\theta)} \left\{ \frac{k_1 R_d}{g_0} P(z_0) + \int_{z_0}^{z_{\text{ref}}} \left[k'_2 \frac{e}{T} + k_3 \frac{e}{T^2} \right] dz \right\} \quad (1)$$

where θ is the incidence angle of the ray. The first term on the right-hand side in Eq. (1) is the hydrostatic delay and is calculated using the specific gas constant for dry air ($R_d = 287.05 \text{ J kg}^{-1} \text{ K}^{-1}$), the gravity acceleration at ground surface ($g_0 = 9.8 \text{ m s}^{-2}$) and the air pressure (P) at the elevation ground level (z_0). The hydrostatic delay, accounting about 90% of the total delay, is approximately 2.3 m in zenith direction but is quite stable in time so when forming the interferogram most of this component are canceled out. The second term relates to the wet delay and is integrated between the ground surface (z_0) and the reference height (z_{ref}) using the partial pressure of water vapor (e) and the absolute air temperature (T). Above the reference elevation z_{ref} (30 km is accepted in this study) the path delay is assumed to be nearly unchanged with time. The atmospheric refractivity constants are from (Smith and Weintraub, 1953) and $k_1 = 0.77604 \text{ K Pa}^{-1}$, $k'_2 = 0.6479 \text{ Pa}^{-1}$, $k_3 = 3.75 \times 10^3 \text{ K}^2 \text{ Pa}^{-1}$. The wet delay represents about 10% of total delay, varying approximately 20–300 mm and varies in random spatially and temporally. We do not account for the influence of the ionosphere because this effect in our C-band SAR test data is minimal (Hanssen, 2001). Given the meteorological parameters such as temperature, pressure, and water vapor partial pressure, Eq. (1) allows one to calculate an estimate of the single-path tropospheric delay for two SAR acquisitions at times t_1 and t_2 , and the delay in an interferogram can be written as,

$$\delta L_{\text{LOS}}^{t_1, t_2}(z) = \delta L_{\text{LOS}}^{\text{total}}(z, t_2) - \delta L_{\text{LOS}}^{\text{total}}(z, t_1) \quad (2)$$

ERA-Interim is the latest Global Atmospheric Model produced by ECMWF which was instigated to address some of the problems seen in ERA-40. It is based on 4-dimensional variational assimilation of global surface and satellite meteorological data. This reanalysis provide global weather estimates of temperature, water vapor partial pressure, and geopotential height along 37 pressure levels, on a global 0.7° grid (~75 km), at 0:00, 6:00, 12:00, and 18:00 UTC daily, from 1979 to present (Dee et al., 2011).

To compute the single-path delay corresponding to the SAR acquisition time t_i , we extracted the vertical profiles of temperature, specific humidity, and geopotential height that is closest to time t_i from ERA-Interim grid points located in an area that encompass the entire SAR scene. Then the hydrostatic and wet delay on each ERA-Interim grid point were computed using Eq. (1). Finally, a spline interpolation along altitude was applied to estimate the delay at the pixel's elevation and a bilinear interpolation in the horizontal direction was used to produce the 2D maps of delay. We then differentiate the 2D maps of delay at each different acquisition times to obtain the simulated tropospheric delay of an interferogram.

2.2. Study area and available data set

Taiyuan basin is located in the center of Shanxi province, China. Affected by anthropogenic extraction of groundwater, severe land subsidence has been found in this region. The basin has a mean elevation of 700 m and is surrounded by mountains with an elevation of up to 3000 m in the east (Taihang Mountains) and the west (Lvliang Mountains), see Fig. 1. Due to this reason, the interferograms are expected to be contaminated by significant stratified APS. Because the land subsidence is concentrated over the flat area of the Taiyuan basin, the deformation signal is not significantly affected by stratified tropospheric effects. However, it is important to remove the stratified APS outside the basin, since it is significant in some interferograms and it can affect the phase estimation in areas assumed without deformation that are used to refer displacement (López-Quiroz et al., 2009). Meanwhile, the subsidence areas in the flat terrain could be affected by the turbulent APS. As a result, atmospheric correction should be applied for accurate measurement of ground deformation in this study area.

A two year ENVISAT archive of 17 SAR images centered on Taiyuan basin was provided by the European Space Agency (ESA). Those SAR acquisitions were

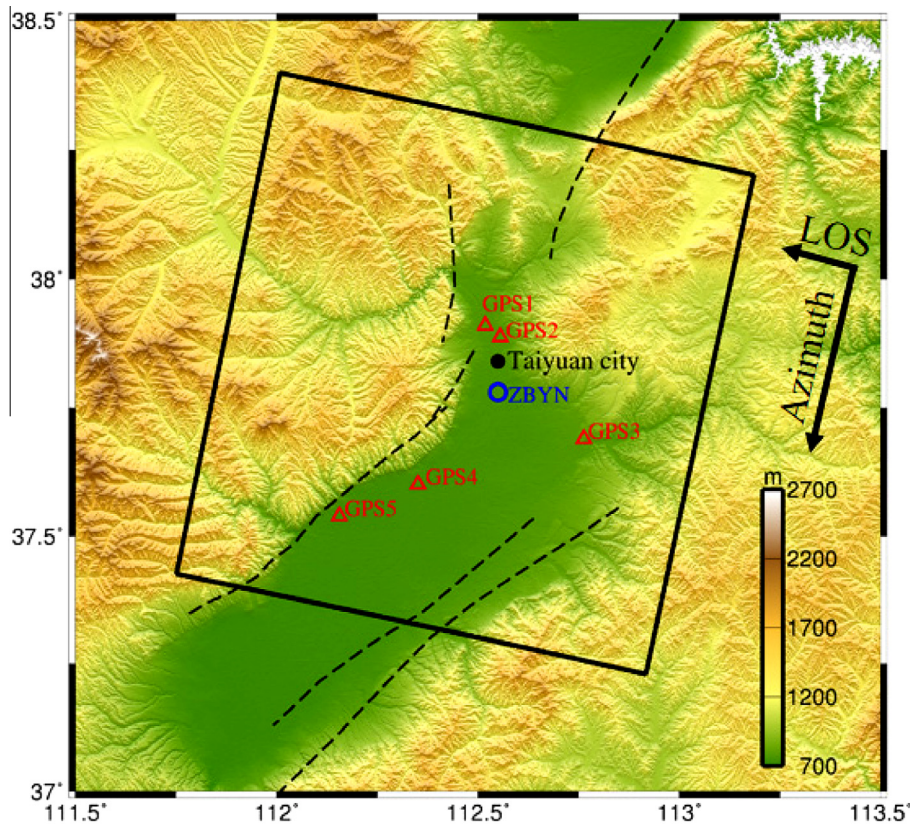


Fig. 1. Topographic map of the study area. The black solid box represents the coverage of ENVISAT ASAR image. The blue circle indicates the radiosonde station while the red triangles represent the 5 continuous GPS stations used in this study. The dashed line shows the major faults in this area. The arrows denoted as the LOS direction and the flight direction (azimuth). (For interpretation of the references to color in this figure legend, the reader is referred to the web version of this article.)

Table 1

ENVISAT ASAR data set baseline information. All interferograms are relative to the master of 17 January 2010.

Date (YYMMDD)	Perpendicular baseline (m)	Temporal baseline (m)	Doppler central baseline (Hz)
20090201	448	350	1.1
20090308	194	315	-11.5
20090412	306	280	1.2
20090621	180	210	4.5
20090726	210	175	-2.1
20090830	154	140	-5.1
20091004	338	105	-4.3
20091108	155	70	-4.4
20091213	642	35	7.4
20100117	0	0	0
20100221	377	35	-4.6
20100328	136	70	-15.1
20100502	27	105	-7.1
20100606	74	140	-12.1
20100711	277	175	-18.8
20100815	162	210	-15.8
20100919	132	245	-10.1

acquired along the descending orbit between February 01 2009 and September 19 2010 and at the time ~02:43 UTC. The image acquired on January 17 2010 was selected as the master scene, the baseline information is shown in Table 1. We used the precise orbit information from Delft Institute for Earth-Oriented Space Research to minimize the orbital errors and the Shuttle Radar Topography Mission (SRTM) digital elevation model (Farr et al., 2007) with a 90 m pixel spacing to remove topographic phase component.

2.3. Accuracy evaluation by radiosonde

The accuracy of the simulated atmospheric delay from the ERA-Interim is essential for evaluating its potential for correcting tropospheric effects in differential SAR interferometry. The accuracy evaluation of the ERA-Interim proceeded in two steps. The first step is a comparison of the vertical profile of the ERA-Interim with radiosonde data. The second approach is the evaluation of the spatial distribution of the atmospheric delay from the ERA-Interim and from the SAR interferograms. The first step is discussed in this section and the second one will be demonstrated in the next section. Only one radiosonde station (ZBYN shown in Fig. 1) is available in our study area. The radiosonde data have been acquired at 00:00 UTC, which is coincident with the time of ERA-Interim reanalysis we used in this study. The vertical distributions of specific humidity estimated from radiosonde and ERA-Interim are shown in Fig. 2. In spite of the limited comparison, the results in Fig. 2 reveal that the water vapor amount from ERA-Interim have reliable absolute values in vertical profiles. The time series of precipitable water vapor (PWV) from radiosonde and ERA-Interim are compared in Fig. 3A, which are reflective of the seasonal oscillation of the wet delay. It can be seen that the amount of PWV

changes seasonally, reaching 3 mm in winter and 50 mm in summer.

Linear regression offers another way of describing the relationship between the PWV derived from radiosonde and ERA-Interim. Assuming the two datasets have the following linear relationship, $\text{ERA-Interim_PWV} = a \times (\text{Radiosonde_PWV}) + b$, the linear regression was performed. As shown in Fig. 3B, if ERA-Interim and radiosonde measurements would provide perfect and unbiased results, the prefect fitting line (the dashed line) should show $a = 1.0$ and $b = 0.0$. The best fitting line can be expressed by $a = 1.03$ and $b = 0.42$ and the line regression standard deviation is $\sigma_{\text{pwv}} = 1.10$ mm. Fig. 3 shows that consistent results between ERA-Interim PWV and radiosonde PWV over ZBYN site as the regression line does not significantly differ from the optimal fit. The comparisons and evaluations suggest that ERA-Interim can obtain water vapor amounts with a reliable accuracy and have a significant potential for correcting tropospheric effects in SAR interferogram.

2.4. Accuracy evaluation by SAR interferograms

For further demonstrating the effectiveness of the atmospheric correction method, the mitigation results to real SAR interferograms are presented and discussed in this section. The effectiveness is evaluated by the standard deviation reduction after atmospheric correction and the delay correlation between interferograms and the ERA-Interim predictions. We expect a high value of standard deviation reduction and a high delay correlation if ERA-Interim performs well.

We selected five interferograms with high coherence as a test case, see Table 2. The DORIS software (Kampes and Usai, 1999) was used for interferometric processing. These interferograms were multilooked by 40 looks in azimuth and 8 looks in range to reduce phase noise and enhance phase unwrapping accuracy. Before phase unwrapping, the adaptive power spectrum filter was applied to improve the signal to noise ratio of the interferogram (Goldstein and Werner, 1998). High-rate land subsidence in several regions have been observed in all of interferograms. These subsiding regions were masked out to avoid mixing the atmospheric signal with surface displacement. Hence, the dominant signal in the differential interferograms will only be the result of atmospheric phase delay.

The standard deviation of original interferograms and the residuals are quantified in Table 2. After correction, interferograms 1, 3, 4 and 5 show significant mitigation that the standard deviations reduce 43%, 58%, 43%, and 51%, respectively. The delay correlation between original interferograms and ERA-Interim simulations for these four interferograms are 0.68, 0.81, 0.78, and 0.80 respectively. Fig. 4 shows the maps of atmospheric corrections for these interferograms. From Fig. 4, we observed that the delay simulations based on ERA-Interim reproduce the phase

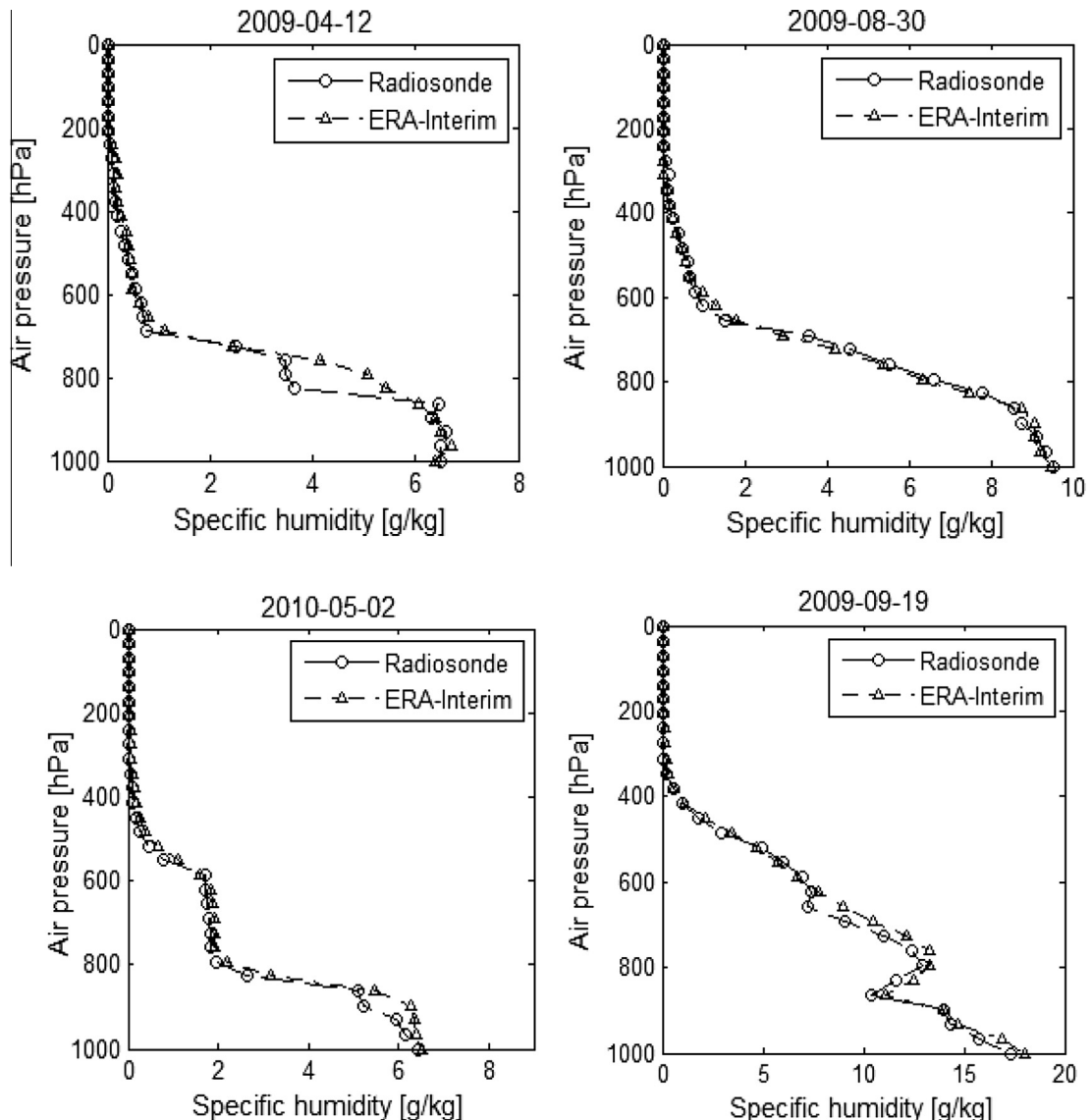


Fig. 2. Accuracy evaluation of specific humidity from the vertical profile of radiosonde and ERA-Interim. The solid line represents the radiosonde measurements, and the dashed line indicates the ERA-Interim reanalysis. The sounding data are provided by the Department of Atmospheric Science of the University of Wyoming (<http://weather.uwyo.edu/upperair/sounding.html>).

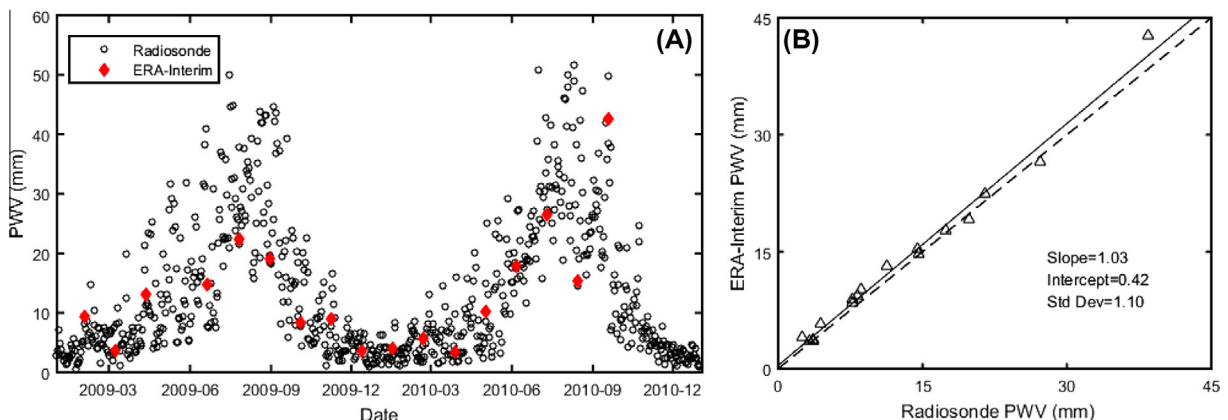


Fig. 3. (A) Time series of the PWV from radiosonde and ERA-Interim; (B) correlation between radiosonde and ERA-Interim PWV estimates; the line of perfect fit (dashed line) and a least square regression line (solid line) are plotted.

Table 2

Mitigation results for differential interferograms. Standard deviation (mm) of the original interferogram and the residual are denoted as σ_{InSAR} and σ_{res} , respectively. γ indicates the delay correlation between the interferometric phase and the ERA-Interim predictions. B_{\perp} and B_t represent the perpendicular and temporal baseline respectively.

Index	Interferogram (date)	B_{\perp}	B_t	σ_{InSAR}	σ_{res}	γ
1	20090830/20091108	30	70	9.56	5.47	0.68
2	20100328/20100502	110	35	4.51	5.23	0.03
3	20100328/20100606	64	70	5.12	2.14	0.81
4	20100502/20100606	46	35	3.72	2.12	0.78
5	20100711/20100815	120	35	7.21	3.52	0.80

delay in the interferograms reasonably well in the spatial pattern. Note that the significant atmospheric phase delay on the mountain areas but a relatively small one is observed in the flat terrain of Taiyuan basin. Finally note the last column of Fig. 4 that how these signals are significantly reduced, suggesting that this delay are strongly correlated with land topography. This can be visualized by plotting phase delay against the local topography as shown in Fig. 5. Strong topography-dependent delay can be observed both in InSAR and ERA-Interim for cases 1, 3, 4 and 5. We modeled the topography-dependent delays by fitting the delays along the elevation using a linear trend (red lines in Fig. 5). The linear relations after removing the ERA-Interim predictions are reduced as can be seen in the last column in Fig. 5. This further suggests that the considerable delay mitigations in these interferograms are largely due to the removal of delay which are correlated with topography. We found that the ERA-Interim slightly overestimated the delay on the mountain areas due to the slope changed from positive to negative on these four interferogram. We also observed that some inconsistencies (dashed red ellipses in Fig. 4) exists on interferogram 1 and interferogram 5, indicating that the short scale component of atmospheric delay cannot be captured by ERA-Interim predictions.

However, for interferogram 2, deterioration is observed for the full interferogram rather than mitigation since the phase standard deviation increased. The delay correlation between interferometric phase and the predicted phase delay is only 0.03. From Fig. 6, we observed that neither InSAR nor ERA-Interim simulation shows visible topography-dependent delay, suggesting low level stratification of troposphere and hence a relatively high level of local tropospheric turbulence. The slope between interferometric phase and elevation is increased after delay correction, indicating no improvement for this interferogram. In such cases, the ERA-Interim cannot reasonably predict the atmospheric turbulence, our method fails to improve the observations.

Although there are some discrepancies between the atmospheric delays from ERA-Interim and the differential interferograms, good agreements at the mountain regions strongly indicate that the stratified APS is well simulated by the ERA-Interim products. However, residual

atmospheric signal can be found in both cases suggesting that the method presented here is not suitable for removing all atmospheric path delays. The residual atmospheric signal after corrected using ERA-Interim were considered as turbulent APS which are random in time, and they can be mitigated using spatial and temporal filtering in further time series analysis.

3. Atmosphere-corrected for InSAR time series analysis

3.1. The modified PSI method

Time series analysis methods such as PSI and small baseline subset (SBAS), or stacking method assume the atmospheric effects spatially correlated but temporally uncorrelated. Under the assumption, high-pass (HP) filtering in time and low-pass (LP) filtering in space can be used to estimate the atmospheric effects in time series reconstruction. However, as the stratified delay is not randomly distributed in space, it cannot be filtered out by spatial filtering. Additionally, the stratified delay shows seasonal variations which are correlated with time. Thus the estimated surface displacements and velocity fields would be biased, leading to misinterpretation of ground deformation. This suggests that spatial-temporal filtering in time series analysis is not an appropriate approach for estimating stratified delay. Therefore, we propose an atmosphere-corrected PSI that the stratified APS are corrected by using ERA-Interim in the time series interferograms. In this paper, the Stanford method for persistent scatterers (StaMPS) was used (Hooper, Segall, 2007). Correcting for the stratified APS does not remove all the atmospheric signal, the residual component (turbulent APS) are considered as random noise in time and mitigated with time-weighted LP filtering applied in the conventional PSI method. Fig. 7 shows the flowchart of the proposed method.

After PS selection using StaMPS, the wrapped phase in interferogram can be written as the sum of five terms (Hooper, Segall, 2007):

$$W\{\phi_{\text{int}}\} = W\{\phi_{\text{def}} + \phi_{\text{stra}} + \phi_{\text{turb}} + \Delta\phi_{\text{orb}} + \Delta\phi_{\text{DEM}} + \phi_n\} \quad (6)$$

where ϕ_{def} is the phase due to surface displacement, ϕ_{stra} and ϕ_{turb} are the phase component of stratified APS and turbulent APS, respectively. $\Delta\phi_{\text{orb}}$ is the residual phase due to satellite orbit inaccuracies, $\Delta\phi_{\text{DEM}}$ is the DEM error, ϕ_n is the noise term, and $W\{\cdot\}$ is the wrapping operator. The phases of surface displacement, atmospheric delay, and orbital error are assumed to be correlated spatially. These term can be estimated by a low-pass filtering in space and subtracted from Eq. (6) gives

$$W\{\phi_{\text{int}} - L^s\{\phi_{\text{int}}\}\} = W\{\Delta\phi_{\text{DEM}} + \phi_n + \delta\} \quad (7)$$

$$\begin{aligned} \delta &= (\phi_{\text{def}} + \phi_{\text{stra}} + \phi_{\text{turb}} + \Delta\phi_{\text{orb}}) \\ &\quad - L^s\{\phi_{\text{def}} + \phi_{\text{stra}} + \phi_{\text{turb}} + \Delta\phi_{\text{orb}}\} \end{aligned} \quad (8)$$

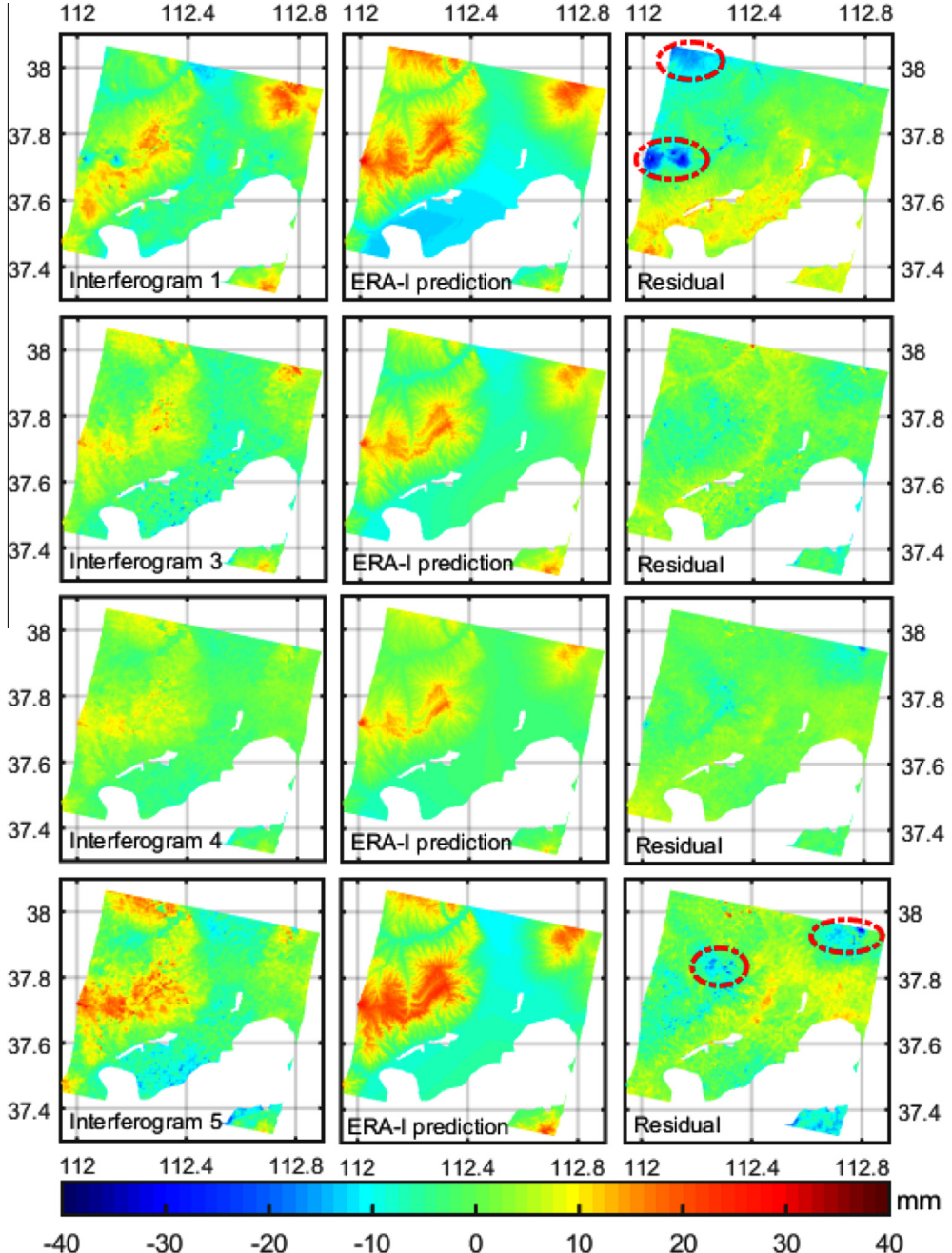


Fig. 4. Stratified atmospheric delay mitigation. The first row (left-to-right) represents the total delay obtained from interferogram 1 in Table 2, the corresponding stratified delay simulated from ERA-Interim, and their difference respectively. The second row, the third row and the last row are the same but for interferogram 3, 4 and 5, respectively. The subsiding regions are masked out. The dashed red ellipses in the figure indicate the locations where there is a large discrepancy between SAR interferograms and ERA-Interim predictions. (For interpretation of the references to color in this figure legend, the reader is referred to the web version of this article.)

DEM error $\Delta\phi_{\text{DEM}}$ is proportionally dependent on the perpendicular baseline and can be written as $\Delta\phi_{\text{DEM}} = \frac{4\pi B_s h \sin \theta}{\lambda R}$. The DEM error is estimated using least square ambiguity deccorrelation (LAMBDA) method (Hooper, Segall, 2007). The stratified phase component ϕ_{stra} is simulated by using the ERA-Interim. Then the DEM error and stratified delay are subtracted,

$$W\{\phi_{\text{int}} - \phi_{\text{stra}} - \Delta\phi_{\text{DEM}}\} = W\{\phi_{\text{def}} + \phi_{\text{turb}} + \Delta\phi_{\text{orb}} + \phi_n + \delta_{\text{stra}}\} \quad (9)$$

where δ_{stra} is the residual between the interferograms and ERA-Interim predictions. Then the phase is unwrapped in three dimension.

$$\phi_{\text{unw}} = \phi_{\text{def}} + \phi_{\text{turb}} + \Delta\phi_{\text{orb}} + \phi_n + \delta_{\text{stra}} \quad (10)$$

By using the low-pass filtering in time, the orbital error and turbulent APS from the master image ($\phi_{\text{turb}}^m + \Delta\phi_{\text{orb}}^m$) can be obtained since the ground deformation at the acquisition of the master image is zero. Superscript m denotes the “master” contribution to these terms.

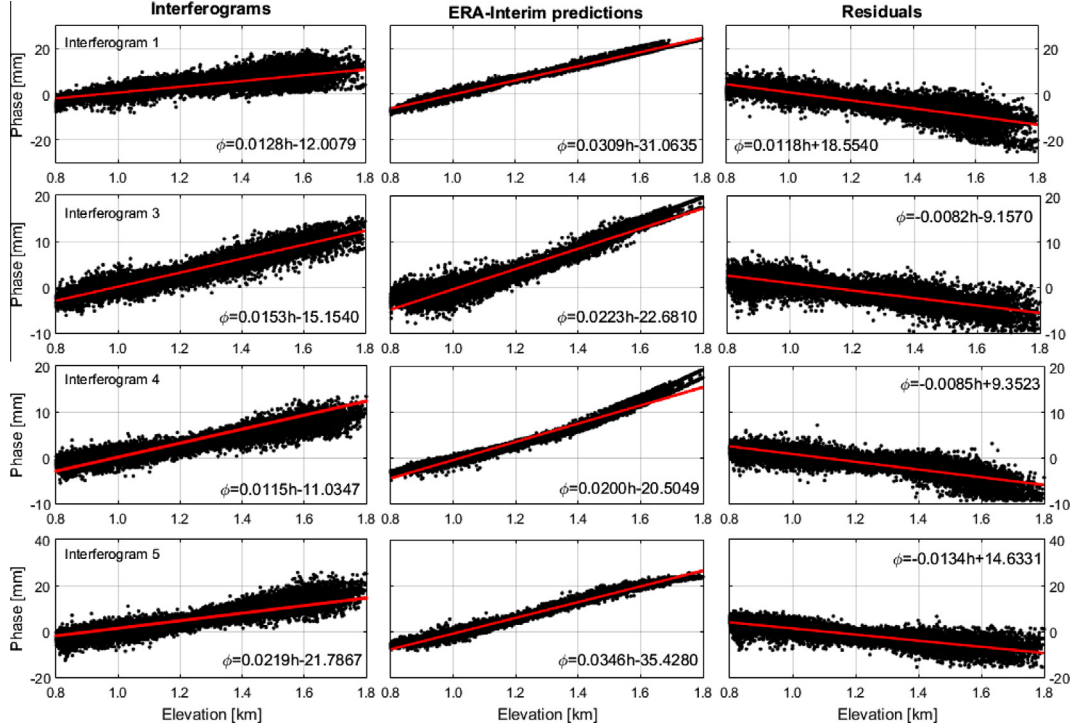


Fig. 5. Phase/elevation plot for the four interferograms in Fig. 4. The first column is the original interferograms. The second column is the corresponding atmospheric delay predicted from ERA-Interim. The last column represents the residuals after removing the corresponding delay. (For interpretation of the references to color in this figure legend, the reader is referred to the web version of this article.)

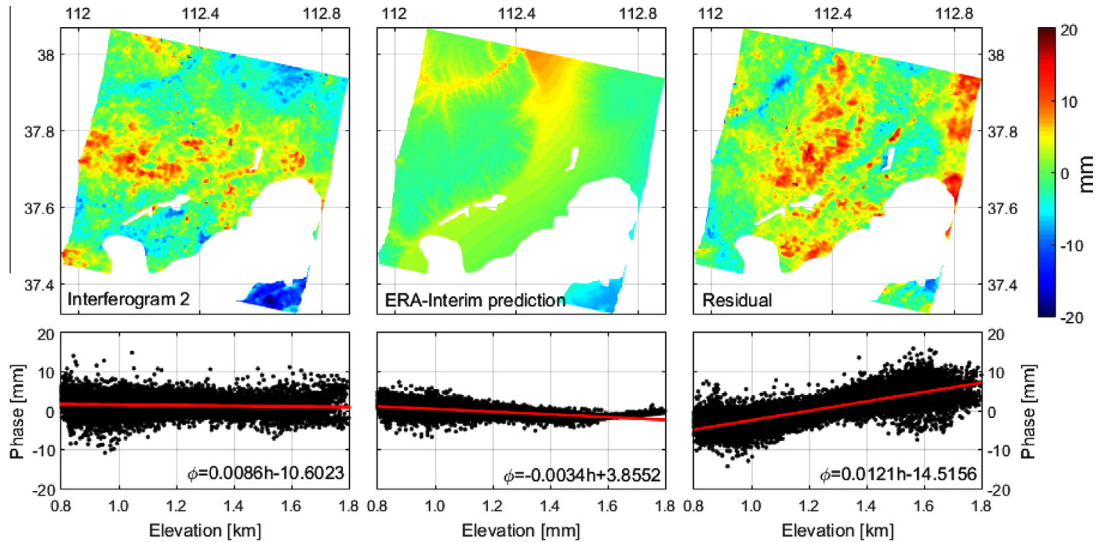


Fig. 6. Turbulent atmospheric delay. The first columns indicate the original interferogram (top) for interferogram 2 in Table 2 and the corresponding phase/elevation plot (bottom). The second column present the delay map predicted using ERA-Interim (top) with corresponding phase/elevation plot (bottom). The third column display the residuals (top) after correction with the ERA-Interim and corresponding phase/elevation plot (bottom).

$$L^T \{\phi_{\text{unw}}\} = \phi_{\text{def}} - \phi_{\text{turb}}^m - \Delta\phi_{\text{orb}}^m + \delta_{\text{stra}} \quad (11)$$

In order to estimate the “slave” contribution to turbulent APS and orbital error, the low-pass filtered signal in Eq. (11) is subtracted from unwrapped phase,

$$\phi_{\text{unw}} - L^T \{\phi_{\text{unw}}\} = \phi_{\text{turb}}^s + \Delta\phi_{\text{orb}}^s + \phi_n \quad (12)$$

where superscript s indicates the “slave” contribution to these terms. Then the atmospheric phase can be achieved by low-pass filtering in space.

$$\phi_{\text{APS}} = L^s \{\phi_{\text{turb}}^s - \phi_{\text{turb}}^m + \phi_{\text{stra}} + \Delta\phi_{\text{orb}}^s - \Delta\phi_{\text{orb}}^m\} \quad (13)$$

Finally, the deformation phase is obtained.

$$\phi_{\text{defo}} = L^s \{\phi_{\text{unw}} - \phi_{\text{APS}}\} \quad (14)$$

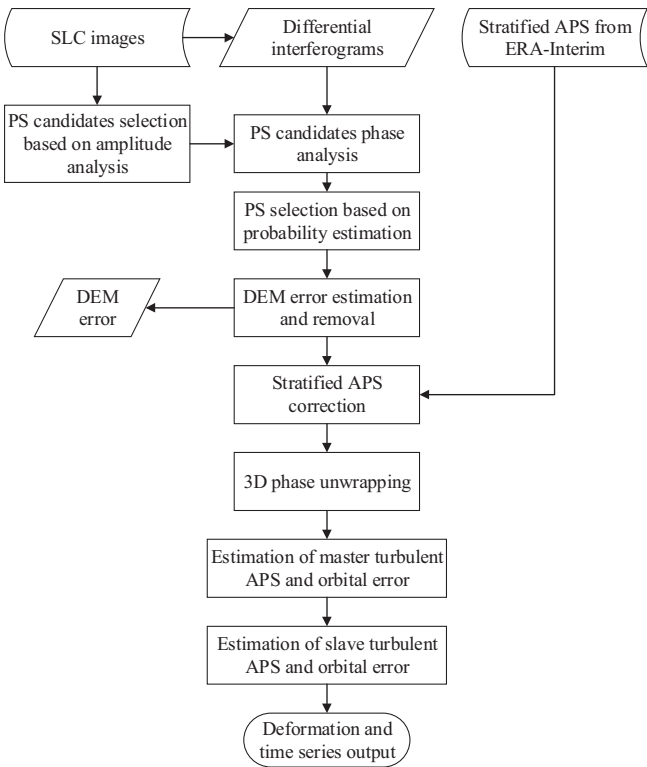


Fig. 7. Flowchart of atmosphere-corrected PSI.

The accuracy of the estimated ground deformation depends on the quality of the simulated stratified delay from ERA-Interim and the amount of turbulent delay in time. In order to minimize the residuals and improve the accuracy of ground deformation, the simulated stratified delay from ERA-Interim should be reliable and sufficient SAR images are required. We will apply this atmosphere-corrected PSI to the time series interferograms in next section.

3.2. Application to Taiyuan ENVISAT ASAR images

In this section, we illustrate the effect of correcting for the stratified APS on the time series of ENVISAT ASAR images covering Taiyuan basin. Ground subsidence represents a major geologic hazard for Taiyuan basin. The subsidence is concentrated over the flat area of the basin. Previous works measuring the subsidence in Taiyuan basin by InSAR focused on the flat area in the basin without accounting for the stratified atmospheric effects on the surrounded mountains (Tang and Liao, 2014; Zhang et al., 2014; Zhu et al., 2013). Although the deformation signal over the flat area of the basin is not significantly affected by stratified delay, it is still important to remove these contributions outside of the basin since it is significant on the mountains (Fig. 4). And it affects the phase estimation in areas assumed without deformation that are used to refer displacement.

As introduced in Section 2.2, 17 ENVISAT ASAR images (Table 1) are available in our study area. The acquisition on January 17 2010 was selected as the common master image and 16 differential interferograms were formed by interferometric processing. We applied time series processing using StaMPS to select PS points. StaMPS identified 751,530 pixels as PS points, accounting for about 1.2% of all pixels. DEM errors were estimated iteratively in the algorithm. As the atmospheric effect is not expected to be correlated with perpendicular baseline, the impact of the atmospheric signal on the estimation of DEM error should not be significant. No matter you do atmospheric correction before or after the estimation of DEM error, the change is still very small, which can be seen from Fig. 8.

After DEM errors correction for PS pixels, stratified APS derived from ERA-Interim was subtracted from each wrapped interferogram and then the corrected interferograms were unwrapped in three dimension (Hooper and Zebker, 2007). The unwrapped time-series interferograms

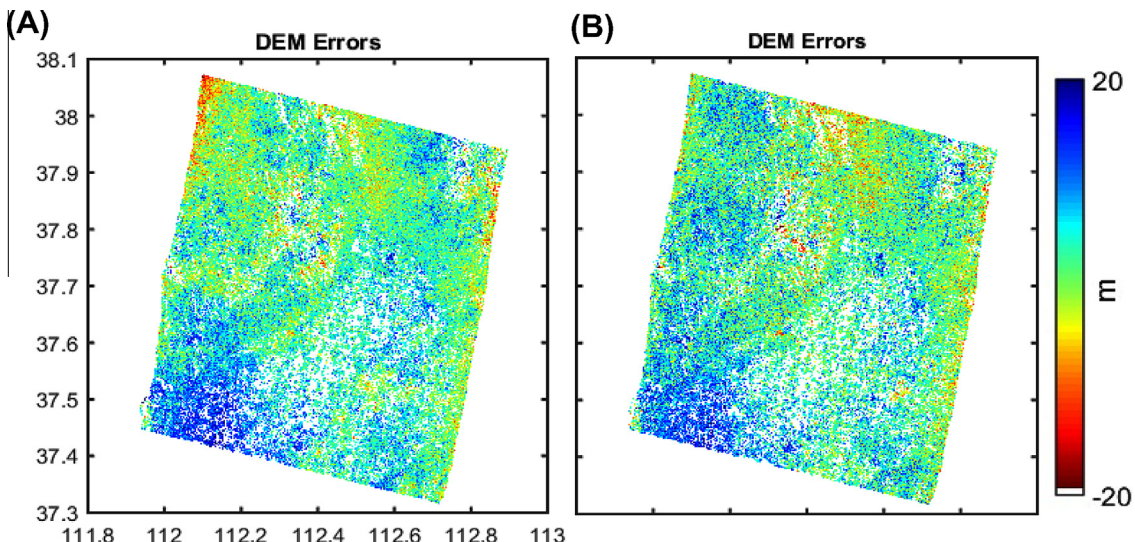


Fig. 8. Line-of-sight (LOS) estimates for DEM errors before (A) and after (B) stratified APS correction.

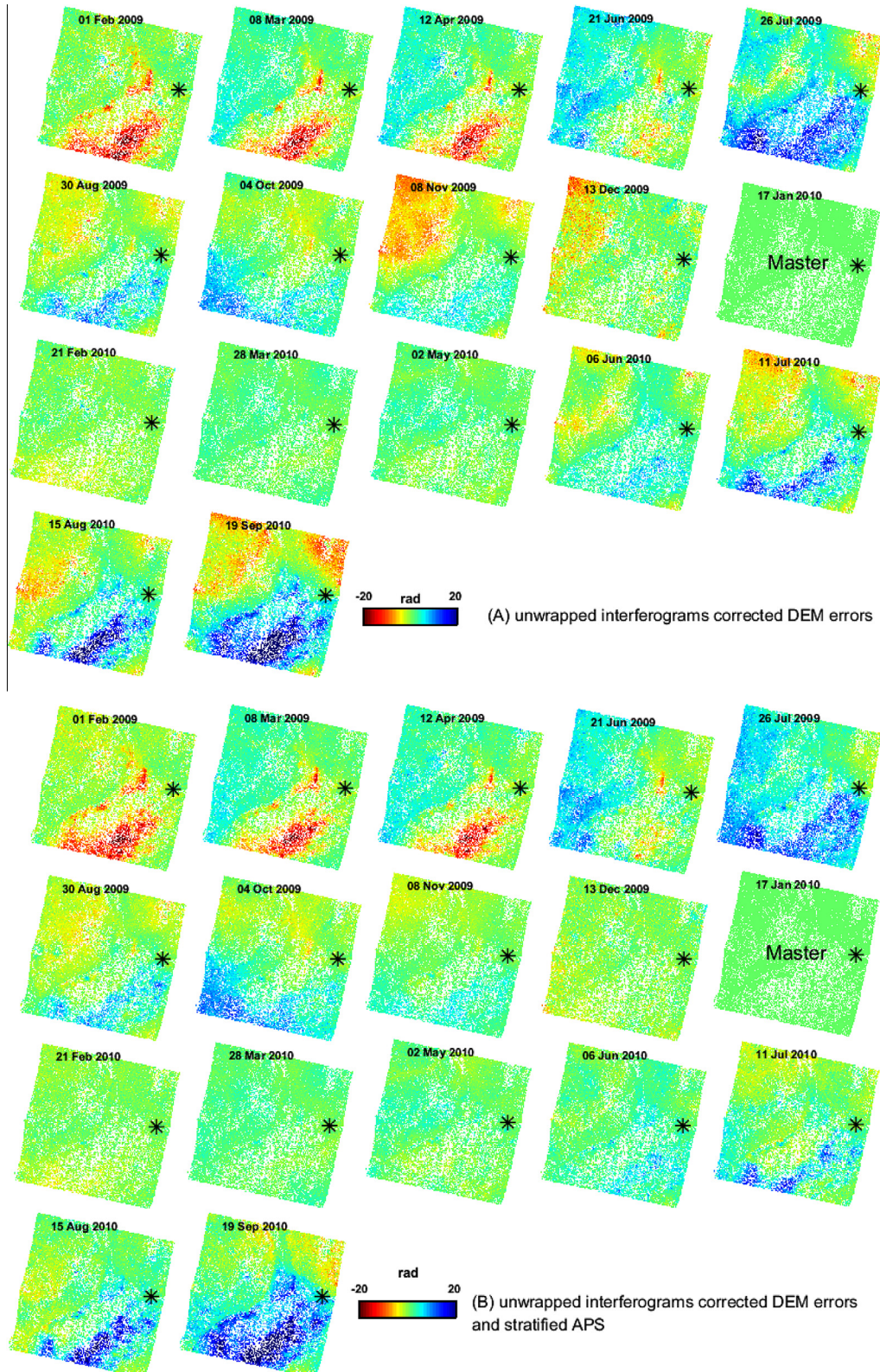


Fig. 9. (A) Unwrapped differential interferograms without stratified APS correction. (B) Unwrapped differential interferograms after removal of the stratified APS. The asterisk represents the center of the circular reference area and the radius of the reference area set to 200 m.

with and without stratified delay correction are shown in Fig. 9. Several regions suffered from severe land subsidence and were observed in the Taiyuan basin. These unwrapped

interferograms (Fig. 9A) without correction of stratified delay contain phases of ground deformation and atmospheric artifacts (including stratified and turbulent

components). In Fig. 9A, it can be observed that interferometric phases on 08 November 2009, 13 December 2009, 06 June 2010, 11 July 2010, 15 August 2010, and 19 September 2010 show strong correlation with surface topography (the topography map see Fig. 1). Note that how the topography-correlated signals are significantly mitigated after stratified APS correction on those interferograms (Fig. 9B). After stratified APS correction, we found an average reduction in local correlation with topography of 3.5 rad/km (~ 1.6 cm/km), with the strongest reductions for interferograms on 08 November 2009 (from 13.2 rad/km to 2.6 rad/km) and on 19 September 2010 (from 10.3 rad/km to 0.01 rad/km). Fig. 10 shows the scatterplots of the correlation between interferometric phase and topography before and after correction of stratified APS for interferograms of 08 November 2009 and 19 September 2010. In total, we find this correction never increase the level noise on the time series interferograms in our study. It suggests that the tropospheric delay simulated from the ERA-Interim significantly mitigate the height-dependent atmospheric effects in the time series differential interferograms.

The remaining signals in unwrapped phases after subtracting the stratified APS are mainly the ground deformation and the small-scale turbulent APS. The turbulent component of APS is randomly in time (high frequency) and spatially correlated in space (low frequency) (Hanssen, 2001), while the deformation signal is temporally correlated. Therefore, we estimated the turbulent APS by

using time-weighted LP filtering as in the conventional PSI. The time window for the time-weighted LP filtering was set at 90 days. The estimated turbulent APS is shown in Fig. 11A. Afterwards, by subtracting the estimated turbulent APS from the interferograms of Fig. 9B, we obtained the interferograms after removal of both stratified and turbulent APS (Fig. 11B).

We then focus on comparisons between the deformation rates over 2009–2010 period obtained with and without correcting for stratified delay using ERA-Interim. Fig. 12A and B show the ground deformation rates estimated by the conventional PSI and by atmosphere-corrected PSI, respectively. Several deforming areas can be identified in Fig. 12. The main differences between both velocity fields are on the Lvliang mountains (upper left side of the image) and in the subsidence area located in the southeastern part of Taiyuan basin. The significant differences on the upper left side are mainly due to stratified APS on the mountainous areas while the minor differences on the flat areas are attributed to the small-scale turbulent APS. The average bias between the velocity fields is ~ 5 mm/year, such variation can result in misinterpretation of ground deformation process. In order to further understand the stratified APS mitigation results at different terrain pattern, we extracted the deformation rate along the profiles P1 – P1', P2 – P2' and P3 – P3' in Fig. 12A which cross the faults from the mountainous terrains to the flat areas, as shown in Fig. 13. The upper maps in Fig. 13 are the topography extracted along those profiles and we

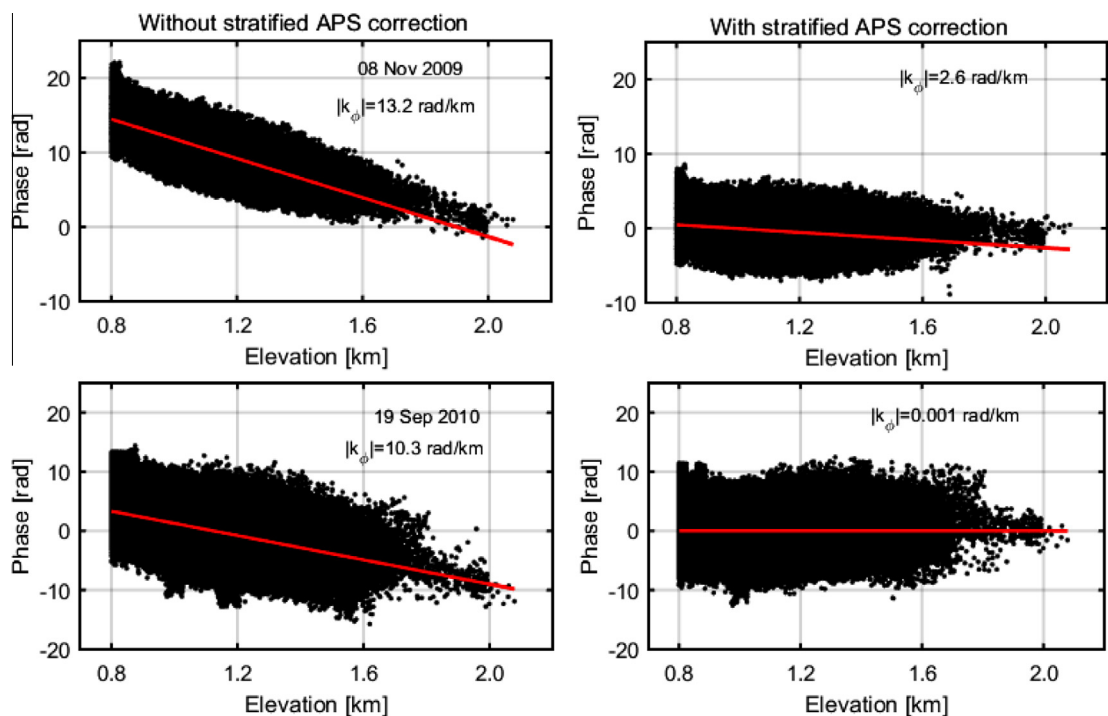


Fig. 10. The scatterplots for the correlation between interferometric phase and topography before and after stratified APS correction for interferograms on 08 November 2009 and 19 September 2010. The black scatters represent the unwrapped phases. The red lines represent the local slope, where $\phi = k_\phi h + \text{constant}$, between the unwrapped phases and the topography. (For interpretation of the references to color in this figure legend, the reader is referred to the web version of this article.)

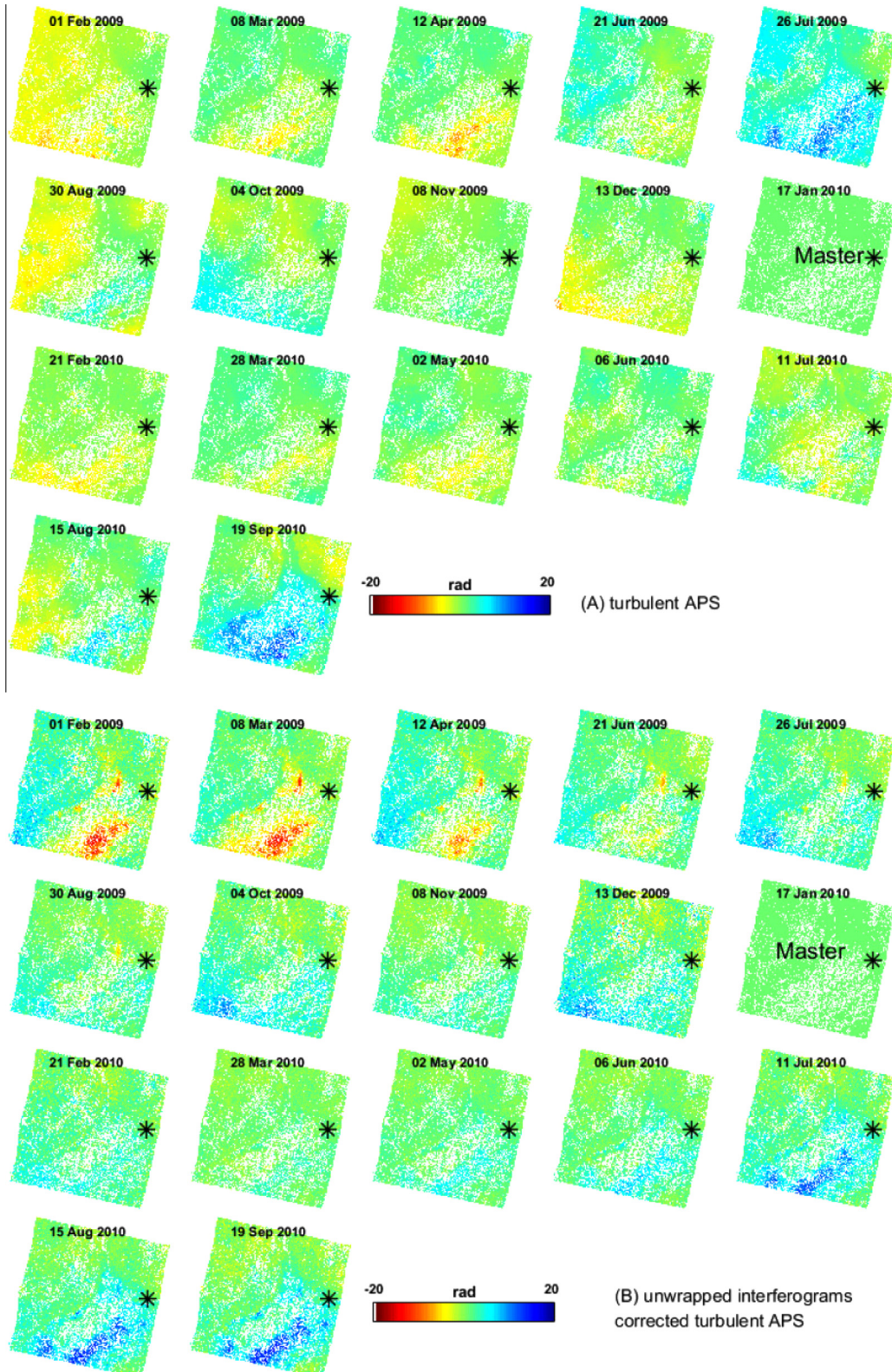


Fig. 11. (A) Estimated turbulent APS by using time-weighted LP filtering. (B) Unwrapped differential interferograms after correction of the turbulent APS by subtracting (A) from interferograms of (B).

observed a strong correlation between the velocity differences and the local topography, suggesting that these errors are attributed to the vertically stratified delay. We also

found from Fig. 13 that the significant stratified effects on the mountains also lead to velocity bias on the flat terrain of Taiyuan basin even though these impacts are small.

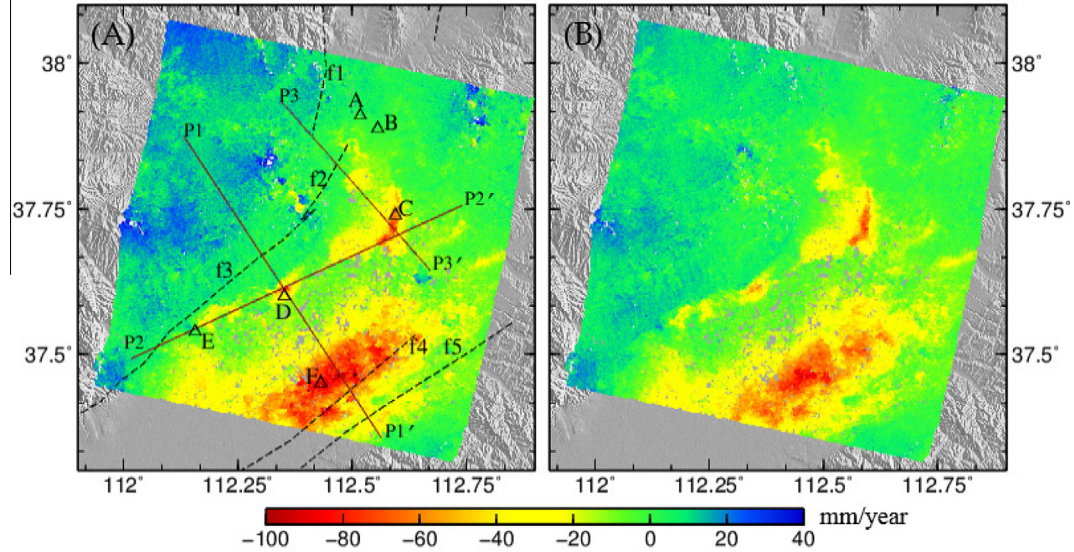


Fig. 12. Mean deformation velocity maps in LOS direction superimposed on the topography of the study area. (A) Mean deformation rates using conventional PSI (StaMPS). Brown solid lines marked with P1 – P1', P2 – P2' and P3 – P3' represent the location of the profiles. Triangles, marked with A, B, C, D, E and F represent the monitoring points of time series of deformation. The dashed line shows the major faults in this area. (B) Mean deformation rates applying atmosphere-corrected PSI proposed in this study. (For interpretation of the references to color in this figure legend, the reader is referred to the web version of this article.)

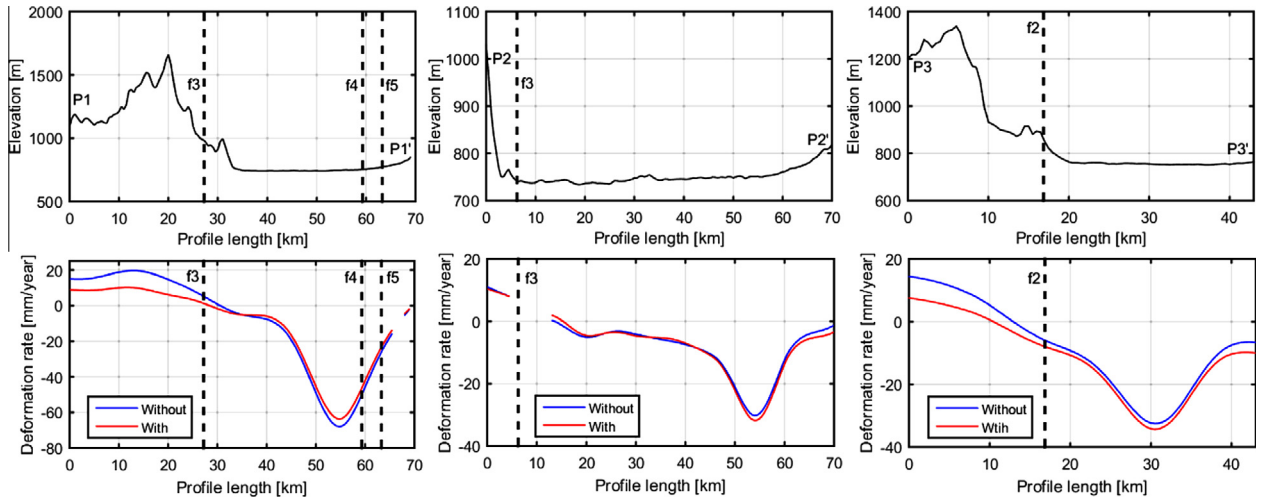


Fig. 13. Collocated profiles of topography (upper map) and LOS deformation rates (lower map) along the profiles in Fig. 12A. The blue and red lines represent deformation rates generated from Fig. 12A and B, respectively. (For interpretation of the references to color in this figure legend, the reader is referred to the web version of this article.)

The magnitude and pattern of deformation along profile P2 – P2' are very similar because this profile across a flat terrain area that the effects of vertically stratified delay are homogeneous in space. To further analyze the atmospheric effects on the velocity field, we plot the velocity values against the pixels elevation in Fig. 14. We found that the velocity values without correcting for stratified APS have a correlation with elevation in Fig. 14A as well as the velocity differences in Fig. 14C. However, with correcting for stratified APS by using ERA-Interim on each interferogram, the correlation between velocity value and elevation disappeared in Fig. 14B. All of these analysis

strongly support that the estimation of stratified APS from ERA-Interim is valid and reliable.

3.3. Validation with GPS measurements

In order to validate the results, we evaluated the accuracy of atmosphere-corrected PSI by comparing InSAR deformation measurements to that of GPS. There are 5 continuous GPS stations located in our study area (Fig. 1). We present the GPS site velocity in three dimension in absolute coordinates ITRF2008 reference frame in Table 3. Station GPS4 (corresponding to D point in

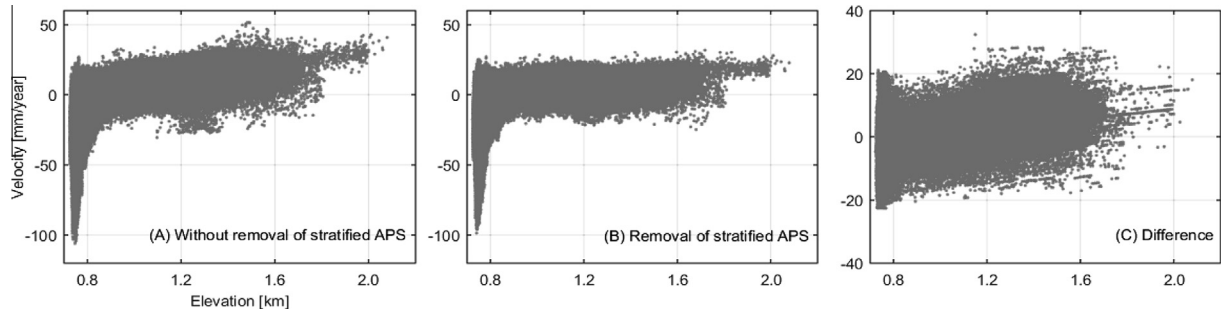


Fig. 14. Deformation velocity plot against pixels elevation. (A) The velocity shown in Fig. 12A as a function of pixels elevation. (B) The velocity shown in Fig. 12B as a function of pixels elevation. (C) The velocity difference between Fig. 12A and B.

Table 3
GPS site velocity in the ITRF2008 reference frame.

GPS stations	North [mm/year]	East [mm/year]	Up [mm/year]
GPS1	-10.06 ± 0.07	31.40 ± 0.07	3.33 ± 0.42
GPS2	-10.06 ± 0.07	31.40 ± 0.07	5.48 ± 0.26
GPS3	-11.13 ± 0.08	32.23 ± 0.08	0.32 ± 0.25
GPS4	-10.17 ± 0.09	29.13 ± 0.09	-32.87 ± 0.33
GPS5	-11.61 ± 0.09	36.86 ± 0.08	-1.11 ± 0.28

Fig. 12A) is located in the area that was subjected to severe land subsidence over the last decade. The other stations are located outside of subsidence areas so that they show relatively small deformation. GPS3 station was selected as the

reference point because it is located on stable ground surface and the position data of other GPS stations were referenced to it. We projected the GPS three dimensional measurements to InSAR LOS direction for comparison. For each GPS station, we selected a subset of PS located nearest to the GPS station to compare the measurements of GPS and PSI. In our study, PS pixels falling within a circular area with a radius 200 m around each GPS station are selected and the actual velocity value for each GPS was derived by averaging using a covariance matrix accounting for the PS coherence values.

In Fig. 15, we show the temporal evolution of displacement from InSAR for six points (see Fig. 12A)

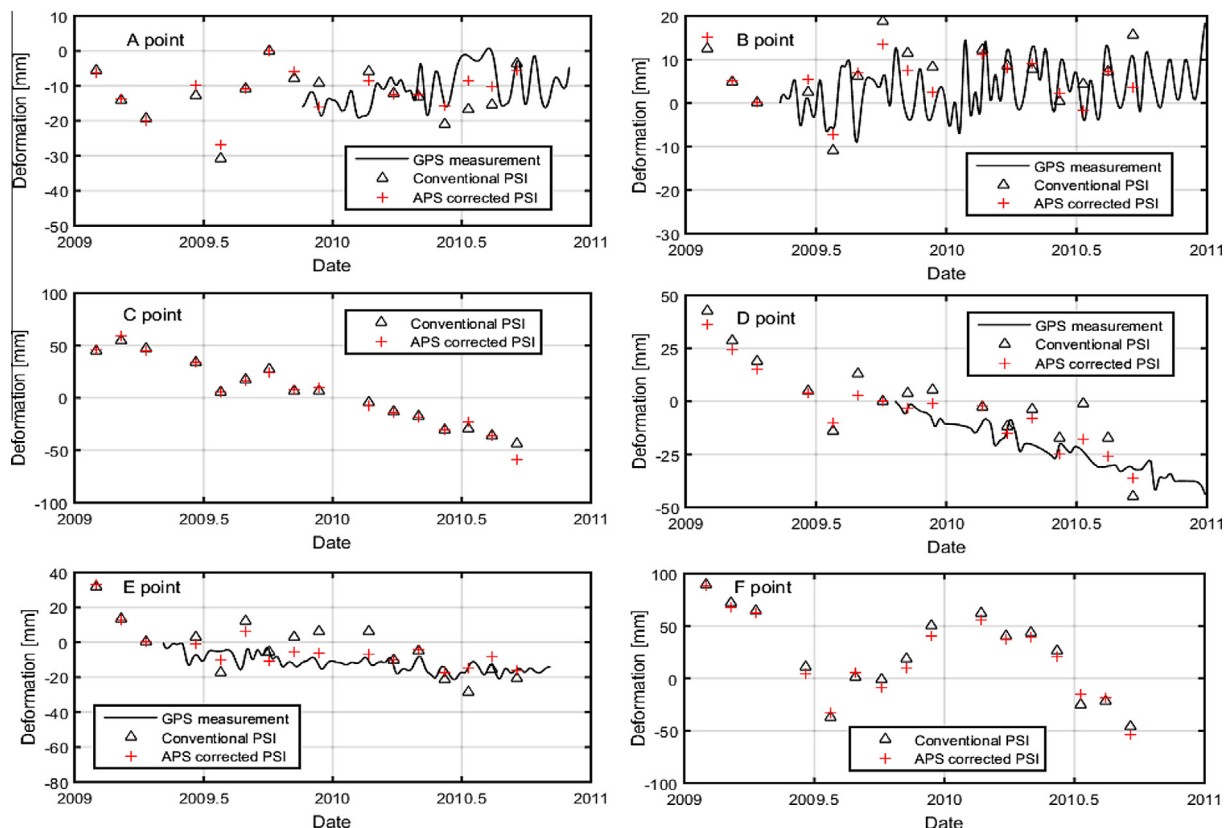


Fig. 15. Temporal variation of deformation for points A–F in Fig. 12A. The black triangles and red crosses represent ground displacement estimated from the conventional PSI and the atmosphere-corrected PSI. For points A, B, D, and E, we have continuous GPS measurements (black line) for comparison. (For interpretation of the references to color in this figure legend, the reader is referred to the web version of this article.)

and compare the time series deformation at points A, B, D, and E to the available GPS displacement at stations GPS1, GPS2, GPS4, and GPS5. Distinct disagreement between the conventional PSI and GPS measurements can be found on those acquisition times (08 November 2009, 13 December 2009, 06 June 2010, 11 July 2010, 15 August 2010, and 19 September 2010) that suffered from severe stratified atmospheric effects, while the atmosphere-corrected PSI give closer ground displacement to that of the GPS. The RMS errors between the measurements from continuous GPS and conventional PSI was 4.8 mm, 5.1 mm, 7.8 mm, and 8.5 mm for points A, B, D, and E, respectively. However, the RMS error decreased to 3.9 mm, 4.2 mm, 5.7 mm, and 5.3 mm, respectively. Even though the atmosphere-corrected PSI also have some errors, this errors are reduced. The differences at points A and B which are located in Taiyuan city are small suggesting that the stratified delay have little impact for the flat urban area. An uplift from September to next February and sharp subsidence from February can be found at points C, D and F, particularly for point F. This variation was likely be related with the seasonal groundwater-level fluctuations.

4. Discussion

Many differential interferograms show topography-correlated fringes, which are due to tropospheric stratification components in the phase. This component of atmospheric phase delay can be significantly removed by ERA-Interim as shown in this study. However, the ERA-Interim likely underperforms due to the coarse resolution of the model output, where values such as atmospheric pressure are averaged over a large area that might span a kilometer or more of elevation change. The low resolution of the ERA-Interim cannot track the details of the atmospheric structure that are important to InSAR. Thus, atmospheric residuals still remain in the interferograms and show a small correlation with topography. Another limitation is that the stratified delay simulated from ERA-Interim in an area without sufficient direct meteorological data do not accurately represent the atmospheric state. Residuals may also be caused by the time differences between ERA-Interim and SAR acquisition times. Our results showed that, in some cases, significant improvements occur (Fig. 4), but the ERA-Interim is just as likely to deteriorate an image as it is to improve it (Fig. 6). It indicates that this method is not suitable for estimating the component of turbulent delay on single interferogram, because of their nonlinear nature and affecting the interferometric phase on a wide range of scales.

Stratified delay is not randomly distributed in space, it cannot be correctly estimated by spatial-temporal filtering in conventional time series analysis. Therefore, we removed the stratified delay from the time series of interferograms by using ERA-Interim, and considered turbulent delay in the unwrapped phases as a random phase in space and time. The deformation results using conventional PSI

without correcting stratified delay bias the velocity fields especially on the mountains. With our atmosphere-corrected PSI, the velocity bias due to stratified APS on the mountains are significantly mitigated. Compared to GPS measurements, the proposed time series method gave a closer deformation to the GPS, suggesting accuracy improvement of our method.

5. Conclusions

Tropospheric stratified delay can induce significant errors in the estimation of ground displacement for InSAR application. In this paper, we corrected this component of atmospheric delay by using global atmospheric reanalysis provided by ERA-Interim. Our results showed that the proposed method improves the differential interferograms by removing the topography-correlated phase delay but it is not suitable for interferograms when turbulent delay dominate the atmospheric signal. Further research is required in order to understand under what circumstances our proposed atmospheric correction method works best. Tropospheric stratified delay also biases the velocity fields when using time series InSAR techniques. Therefore, atmosphere-corrected PSI method was proposed. We applied the atmosphere-corrected PSI to the ENVISAT time series of SAR images to study land subsidence in Taiyuan basin. Our results showed that the differences of the velocity fields between the conventional PSI and atmosphere-corrected PSI mainly occurred on high relief terrains. However, the differences are very small at the flat terrain of the urban area. Our results were validated with continuous GPS measurements and demonstrated that the deformation accuracy of atmosphere-corrected PSI was improved.

Acknowledgements

The authors thank ESA for the ENVISAT ASAR images. This project was supported by the National Key Basic Research Program of China (Grant No. 2013CB733205) and the National Natural Science Foundation of China (Grant Nos. 61331016 and 41571435). I would also like to thank Stephen C. McClure for his helpful comments and suggestions on this manuscript.

References

- Baby, H., Golé, P., Lavergnat, J., 1988. A model for the tropospheric excess path length of radio waves from surface meteorological measurements. *Radio Sci.* 23, 1023–1038.
- Berardino, P., Fornaro, G., Lanari, R., Sansosti, E., 2002. A new algorithm for surface deformation monitoring based on small baseline differential SAR interferograms. *IEEE Trans. Geosci. Remote* 40, 2375–2383.
- Cavalie, O., Doin, M.P., Lasserre, C., Briole, P., 2007. Ground motion measurement in the Lake Mead area, Nevada, by differential synthetic aperture radar interferometry time series analysis: probing the lithosphere rheological structure. *J. Geophys. Res.* 112.

- Colesanti, C., Wasowski, J., 2006. Investigating landslides with space-borne synthetic aperture radar (SAR) interferometry. *Eng. Geol.* 88, 173–199.
- Dee, D.P., Uppala, S.M., Simmons, A.J., et al., 2011. The ERA-Interim reanalysis: configuration and performance of the data assimilation system. *Q. J. R. Meteorol. Soc.* 137, 553–597.
- Doin, M.P., Lasserre, C., Peltzer, G., Cavalié, O., Doubre, C., 2009. Corrections of stratified tropospheric delays in SAR interferometry: validation with global atmospheric models. *J. Appl. Geophys.* 69, 35–50.
- Farr, T.G., Rosen, P.A., Caro, E., et al., 2007. The shuttle radar topography mission. *Rev. Geophys.* 45.
- Ferretti, A., Prati, C., Rocca, F., 2001. Permanent scatterers in SAR interferometry. *IEEE Trans. Geosci. Remote* 39, 8–20.
- Goldstein, R.M., Werner, C.L., 1998. Radar interferogram filtering for geophysical applications. *Geophys. Res. Lett.* 25, 4035–4038.
- Hanssen, R., 2001. Radar interferometry. In: *Data Interpretation and Error Analysis*. Delft Univ. Technol., Delft, The Netherlands.
- Hooper, A., Zebker, H.A., 2007. Phase unwrapping in three dimensions with application to InSAR time series. *J. Opt. Soc. Am.* 24, 2737–2747.
- Hooper, A., Segall, P., Zebker, H., 2007. Persistent scatterer interferometric synthetic aperture radar for crustal deformation analysis, with application to Volcán Alcedo Galápagos. *J. Geophys. Res.* 112.
- Jolivet, R., Grandin, R., Lasserre, C., Doin, M.P., Peltzer, G., 2011. Systematic InSAR tropospheric phase delay corrections from global meteorological reanalysis data. *Geophys. Res. Lett.* 38.
- Kampes, B., Usai, S., Doris, 1999. The delft object-oriented radar interferometric software. In: *2nd International Symposium on Operationalization of Remote Sensing*. Citeseer, Enschede, the Netherlands.
- Lanari, R., Lundgren, P., Sansosti, E., 1998. Dynamic deformation of Etna Volcano observed by satellite radar interferometry. *Geophys. Res. Lett.* 25, 1541–1544.
- Li, Z.H., Muller, J.P., Cross, P., Fielding, E.J., 2005. Interferometric synthetic aperture radar (InSAR) atmospheric correction: GPS, moderate resolution Imaging spectroradiometer (MODIS), and InSAR integration. *J. Geophys. Res.* 110.
- Li, Z., Fielding, E.J., Cross, P., Muller, J.-P., 2006a. Interferometric synthetic aperture radar atmospheric correction: GPS topography-dependent turbulence model. *J. Geophys. Res.* 111.
- Li, Z., Fielding, E.J., Cross, P., Muller, J.-P., 2006b. Interferometric synthetic aperture radar atmospheric correction: medium resolution imaging spectrometer and advanced synthetic aperture radar integration. *Geophys. Res. Lett.* 33.
- López-Quiroz, P., Doin, M.-P., Tupin, F., Briole, P., Nicolas, J.-M., 2009. Time series analysis of Mexico City subsidence constrained by radar interferometry. *J. Appl. Geophys.* 69, 1–15.
- Massonnet, D., Holzer, T., Vadon, H., 1997. Land subsidence caused by the East Mesa geothermal field, California, observed using SAR interferometry. *Geophys. Res. Lett.* 24, 901–904.
- Onn, F., Zebker, H.A., 2006. Correction for interferometric synthetic aperture radar atmospheric phase artifacts using time series of zenith wet delay observations from a GPS network. *J. Geophys. Res.* 111.
- Smith, E.K., Weintraub, S., 1953. The constants in the equation for atmospheric refractive index at radio frequencies. *Proc. IRE* 41, 1035–1037.
- Tang, W., Liao, M., 2014. Taiyuan City subsidence observed with Persistent Scatterer InSAR. *Wuhan Univ. J. Nat. Sci.* 19, 526–534.
- Zebker, H.A., Rosen, P.A., Goldstein, R.M., Gabriel, A., Werner, C.L., 1994. On the derivation of coseismic displacement fields using differential radar interferometry: the Landers earthquake. *J. Geophys. Res.: Solid Earth* 99, 617–634.
- Zhang, Q., Zhu, W., Ding, X., Zhao, C., Yang, C., Qu, W., 2014. Two-dimensional deformation monitoring over Qingxu (China) by integrating C-, L- and X-bands SAR images. *Remote Sens. Lett.* 5, 27–36.
- Zhu, W., Zhang, Q., Ding, X., Zhao, C., Yang, C., Qu, W., 2013. Recent ground deformation of Taiyuan basin (China) investigated with C-, L-, and X-bands SAR images. *J. Geodyn.* 70, 28–35.